



Published in final edited form as:

Magn Reson Med. 2014 December ; 72(6): 1499–1508. doi:10.1002/mrm.25061.

Influence of Bone Marrow Composition on Measurements of Trabecular Microstructure using Decay due to Diffusion in the Internal Field (DDIF) MRI: Simulations and Clinical Studies

Sara M. Sprinkhuizen¹, Jerome L. Ackerman¹, and Yi-Qiao Song^{1,2}

¹Athinoula A. Martinos Center for Biomedical Imaging, Department of Radiology, Massachusetts General Hospital, 149 13th Street, Charlestown, MA 02129 USA

²Schlumberger-Doll Research, 1 Hampshire Street, Cambridge, MA 02139 USA

Abstract

Purpose—Decay due to Diffusion in the Internal Field (DDIF) MRI allows for measurements of microstructures of porous materials at low spatial resolution and thus has potential for trabecular bone quality measurements. In trabecular bone, solid bone changes (osteoporosis) as well as changes in bone marrow composition occur. The influence of such changes on DDIF MRI was studied by simulations and *in vivo* measurements.

Methods—Monte Carlo simulations of DDIF in various trabecular bone models were conducted. Changes in solid bone and marrow composition were simulated with numerical bone erosion and marrow susceptibility variations. Additionally, *in vivo* measurements were performed in the lumbar spine of healthy volunteers of ages 23 to 62 years.

Results—Simulations and *in vivo* results yielded that 1) DDIF decay times decrease with increasing marrow fat and 2) the marrow fat percentage needs to be incorporated in the DDIF analysis to discriminate between healthy and osteoporotic solid bone structures.

Conclusions—Bone marrow composition plays an important role in DDIF MRI: incorporation of marrow fat percentage into DDIF MRI allowed for differentiation of young and old age groups (*in vivo* experiments). DDIF MRI may develop into a means of assessing osteoporosis and disorders that affect marrow composition.

Keywords

Trabecular bone; Marrow; Osteoporosis; Stimulated echo; Diffusion; Monte Carlo

Introduction

In osteoporosis, bone loss is reflected in microstructural changes of trabecular bone (1). The primary screening method for osteoporosis, dual energy x-ray absorptiometry (DXA) (2), provides no information on bone microstructure, since it assesses only the spatially averaged

Corresponding Author: Sara Maria Sprinkhuizen, PhD, Athinoula A. Martinos Center for Biomedical Imaging, Department of Radiology, Massachusetts General Hospital, 149 13th Street, Charlestown, MA 02129 USA, Phone: 617-726-0324, sara@nmr.mgh.harvard.edu.

bone mineral density. It has been shown that DXA mineral density scores have only a modest predictive value for fracture risk, poor predictive value for treatment response, and are subject to artifacts and errors (3-6). Characterization of the microstructure of trabecular bone may therefore lead to more accurate diagnosis of metabolic bone disease and an improved overall predictor of fracture risk and treatment response.

Although the true volumetric 3D mineral density and microarchitecture of bone can be measured with quantitative or peripheral μ CT, this method involves a significant radiation dose. Magnetic resonance imaging (MRI) is a noninvasive imaging modality which does not use ionizing radiation and would therefore allow more frequent screening of patients. High resolution MRI techniques have been developed for direct imaging of bone microstructure (7-12), but these measurements are challenging in terms of achievable spatial resolution and signal-to-noise ratio. Additionally, partial volume effects (leading to under or overestimation of histomorphometric parameters) and subject motion may compromise direct imaging of trabecular structure.

An MRI technique which provides collective information on the microarchitecture of porous materials at lower spatial resolution, in which the pore structure is not spatially resolved, is the Decay due to Diffusion in the Internal Field (DDIF) technique (13,14). DDIF MRI allows for bone microstructure measurement by probing the diffusion of water protons through the pore space of trabecular bone. The DDIF effect is based on the magnetic susceptibility difference between the fluid-filled pore spaces and solid parts or other non-equivalent phases of a porous material, which induces a spatially varying magnetic field in the pores, referred to as the internal field (15). Diffusive motion of the water molecules through the internal field gradients leads to irreversible dephasing. The geometry (size, shape and orientation) of pores as well as the overall susceptibility distribution influences the internal magnetic field distribution and hence the dephasing. DDIF encodes this information as the MR signal response to these statistical distributions (13,14,16). Since DDIF effectively reflects statistical measures of the trabecular microarchitecture, resolving individual trabeculae in the image is not required (17). This diminishes the need for high spatial resolution and permits DDIF to be performed on very low cost compact MRI scanners designed for peripheral imaging, thus holding out the potential of being adopted as a screening method.

The application of DDIF in the differentiation of microstructures and its correlation with μ CT measurements has been demonstrated in bovine trabecular bone specimens in which bone marrow has been replaced with water (17,18). *In vivo*, the bone marrow in the trabecular pores will give rise to multiple complicating factors in the assessment of microstructure using DDIF. Bone marrow is a complex tissue that contains substantial amounts of water and lipid. The amount of fat in marrow is highly variable and depends on the anatomical location, body weight, gender, race, age and bone quality (19-26). Fat molecules have a significantly lower diffusion coefficient than water and therefore do not exhibit the DDIF effect. In addition, fat has a magnetic susceptibility that differs from both solid bone and water ($\chi_{\text{solid bone}} = -11.3$ ppm (27), $\chi_{\text{water}} = -9.04$ ppm (28), $\chi_{\text{fat}} = -7.79$ ppm (27)). The field gradients in the pore spaces therefore depend not only on the microstructure of the solid bone but also on the water-fat ratio and spatial distribution of the

bone marrow within the pores. A study at 4.7 T of *ex vivo* animal bone specimens containing marrow showed differences in the DDIF effect between specimens of different trabecular composition (29).

In pursuing the goal of translating the DDIF technique into clinical practice, the present study characterized trabecular bone using DDIF MRI. The influences of changes in the microstructure of the solid bone as well as changes in the composition of the bone marrow on the DDIF signal were investigated by means of simulations and scanning of human subjects. The simulations permitted a wide range of realistic and hypothetical solid bone structures and bone marrow compositions to be analyzed with the DDIF technique. For the *in vivo* measurements, the simplest correlate of trabecular bone quality was chosen: subject age. *In vivo* DDIF MRI scans were performed on a clinical 3.0 T MRI scanner in the lumbar spine of healthy volunteers ranging in age from 23 to 62 years.

Theory

DDIF pulse sequences are based on the STimulated Echo (STE) sequence and consist of a series of three successive 90° radiofrequency (RF) pulses (30). The DDIF sequence can be divided into three time periods. The first period, between RF pulses 1 and 2, is the first encoding time, T_{enc} . During this period, the transverse magnetization component of the proton spins dephases due to diffusion in the spatially varying internal magnetic field B_i of the pores. The phase accumulation during T_{enc} is given by:

$$\Delta\phi = \gamma \int_0^{T_{enc}} B_i(x(t)) dt \quad [1]$$

where γ is the gyromagnetic ratio for protons and $x(t)$ describes the random walk of the proton in the pore space. The second period between the RF pulse 2 and 3 is called the mixing time, T_M . During this period, the transverse component of the precessing magnetization is stored in the longitudinal direction and spins travel in the pore space by diffusion for a duration T_M , but accumulate no additional phase. The third period is the second encoding time where rephasing occurs as again described by Eq. 1 (with the sign of time reversed) for those spins for which B_i has remained static during all three periods (that is, if no diffusion through field gradients has occurred). At a time interval of T_{enc} after the third pulse, the stimulated echo occurs. Spins which do not rephase fully (because they have diffused through field gradients) are lost to the echo. The echo amplitude therefore encodes the history of the diffusion pathway, and thereby carries information on the architecture of the pore space (13,14,16). The DDIF technique involves the acquisition of a stimulated echo for a range of mixing times and records the MR signal decay as a function of the mixing time. DDIF MR can be carried out in spectroscopic or imaging mode.

The contribution of diffusion in the internal field is not the only factor causing the DDIF signal decay. Both longitudinal relaxation and additional diffusion weighting caused by the imaging gradients G_s that are applied for duration t_G influence the STE amplitude. The DDIF signal decay can be described by (17):

$$S_{DDIF}(T_M) \approx \frac{M_0}{2} \sin^3 \alpha \cdot e^{-\left(\frac{1}{T_{DDIF}}\right)T_M} \quad [2]$$

here M_0 is the equilibrium MR signal for 90° pulses and no relaxation or diffusion effects, α is the flip angle of the three RF pulses, and T_{DDIF} is the overall DDIF signal decay time, given by:

$$\frac{1}{T_{DDIF}} = \frac{1}{T_1} + \frac{1}{T_s} + \frac{1}{T_{int}} \quad [3]$$

Here, T_1 is the longitudinal relaxation, T_s is the contribution of the sequence gradients

($\frac{1}{T_s} = \gamma^2 G_s^2 D t_G^2$ with D the diffusion coefficient), and T_{int} is the contribution of the internal field to the DDIF effect. For diffusion distances smaller than the pore size the contribution of the internal field can be characterized by an internal field gradient G_i , and its contribution

can be approximated by the mean squared of G_i : $\frac{1}{T_{int}} = \gamma^2 G_i^2 D T_{enc}^2$.

To maximize the sequence's sensitivity to the effects of the internal magnetic field gradients and thus to the trabecular structure, it is essential to minimize the dephasing effects caused by the imaging gradients in the sequence. If required, T_1 and T_s can be measured and removed from the overall DDIF rate to yield the intrinsic DDIF rate which is dependent only on the tissue and on the B_0 magnitude and direction.

Methods

Monte Carlo Simulations

Trabecular bone models—Monte Carlo simulations of the DDIF decay were performed to study the influence of solid bone changes as well as marrow composition changes on the outcome of the DDIF technique. Simulations were carried out using two solid bone models (healthy and osteoporotic) in combination with three marrow models with different fat content (low, medium and high marrow fat percentage).

The healthy and osteoporotic solid bone models were based on a 3D μ CT scan of a trabecular bone specimen cut from a previously frozen veal (young bovine) femur (cylindrical sample, 4 cm length, 2 cm diameter, J Carter Veal Company). A μ CT data set was acquired at an isotropic voxel size of 20 μ m, integration time of 250 ms, tube voltage and current of 55 KVp and 145 μ A respectively, while applying a 1200 mg cm^{-3} hydroxyapatite beam hardening correction (μ CT 40, Scanco Medical AG, Brüttisellen, Switzerland). A binary trabecular bone model of size $10.24 \times 10.24 \times 10.24 \text{ mm}^3$ was generated from the μ CT data after removing soft tissues using a threshold. This model served as the healthy trabecular bone model. In addition, an osteoporotic version of this model was generated by 2D binary erosion of every slice with the number of adjacent background pixels necessary for pixel removal set to 1 (ImageJ 1.45s). The microstructural properties (bone volume fraction, surface to volume ratio, trabecular thickness, trabecular

number and trabecular separation) of the two 3D bone models were determined using MicroView (Version 2.1.2, GE Healthcare). The outcome of this is shown in Table 1 and confirms that the erosion model produces a structural result roughly in accord with what we expect in the evolution of healthy bone into osteoporotic bone.

The influence of bone marrow composition was modeled by altering the magnetic susceptibility in the pore space for three fat percentages: low ($\chi_{\text{marrow, 0\% fat}} = -9.04$ ppm), medium ($\chi_{\text{marrow, 50\% fat}} = -8.4$ ppm) and high ($\chi_{\text{marrow, 100\% fat}} = -7.79$ ppm).

Magnetic field and magnetic field gradient calculations—Magnetic field calculations in the trabecular bone models were performed using a Fourier-based method which calculates the magnetic field distribution from a given magnetic susceptibility distribution, as described in detail in previously published work (31). The magnetic susceptibility of solid bone was set to $\chi_{\text{solid bone}} = -11.3$ ppm for all calculations (27). The magnetic susceptibility of the pore spaces depended on the specific marrow composition model described above. Smoothing of the magnetic susceptibility distributions with a $3 \times 3 \times 3$ box kernel was performed prior to the Fourier-based calculations to avoid sharp intensity jumps which hamper the magnetic field calculations. Subsequently, the magnetic field distribution was calculated from this susceptibility distribution (31).

As shown by Eq. 3, the spatial distribution of magnetic field gradients in the pore spaces is of importance for the DDIF effect. It has been shown that the regions with the strongest gradients are found close to the trabecular walls (17,18). To assess the influence of changes in trabecular bone structure and marrow on the magnetic gradient distributions, the absolute field gradient was calculated at every voxel for all six models (normal or osteoporotic \times 3 marrow compositions). Starting on the solid bone surface and moving into the pore space, 4 layers of 1 voxel width were defined. For all layers, the total field gradient distribution was determined and visualized in a histogram.

Monte Carlo simulations—Monte Carlo software was written in MATLAB (Mathworks, Natick, MA, USA) and verified by calculation of the spin echo signal from phase accumulation caused by diffusion of protons in a linear gradient, which was compared to the theoretical result: $S \sim \exp(-\gamma^2 G^2 D T E^3 / 12)$ (32). This test showed that the spatial resolution needed for the simulations was on the order of $10^{-3} \times 10^{-3} \times 10^{-3}$ mm³. Therefore, the center 100^3 voxels of the solid binary bone model as well as the magnetic field map was linearly interpolated to a $2 \times 2 \times 2$ mm³ volume with 1000^3 voxels so as to achieve a spatial resolution of $0.002 \times 0.002 \times 0.002$ mm³. Random walks with a total duration of 1 second with a temporal resolution of 0.2 ms were simulated for a total of 15,000 protons. The starting positions of the protons were randomly chosen within the pore space in the center $1 \times 1 \times 1$ mm³ of the volume. Protons were allowed to diffuse in the pore spaces of the whole $2 \times 2 \times 2$ mm³ volume. Random walks were confined to the pore space by recalculation of the random walk from the time point at which a solid bone region was encountered. The diffusion coefficient was set to 0.5×10^{-3} mm²/sec (33) and in all simulations the main magnetic field strength was set to $B_0 = 1.5$ T.

Subsequently, the signal decay was calculated for a range of mixing times ($T_M = 10$ ms to $T_M = 900$ ms at 5 ms intervals) and $T_{enc} = 20$ ms using:

$$S_{B_i}(T_M) = \frac{1}{N} \sum_{n=1}^N \exp \left(i \cdot \gamma \int_0^{T_{enc}} B_i(x_n(t)) dt + \gamma \int_{T_{enc}+T_M}^{2T_{enc}+T_M} B_i(x_n(t)) dt \right) \quad [4]$$

where S_{B_i} denotes the signal decay due to the internal field, N is the total number of protons ($N = 15,000$) and $x_n(t)$ is the random walk over time of a single proton n . Since S_{B_i} contains effects due to susceptibility induced magnetic field distributions only, longitudinal relaxation effects were incorporated in the signal decay over T_M by multiplication with $\exp(-T_M/T_1)$ where T_1 was taken to be the average of the *in vivo* T_1 of the marrow water of all subjects (1265 ms):

$$S_{DDIF}(T_M) = S_{B_i}(T_M) \cdot e^{-\frac{T_M}{T_1}} \quad [5]$$

The process regarding Monte Carlo simulations in bone models is illustrated in Figure 1.

In vivo DDIF MRI

Subjects—All human subject scanning was conducted in strict conformance to an approved Partners HealthCare institutional review board protocol. A total of 10 healthy volunteers were recruited and scanned. Trabecular bone quality is known to correlate with age. We therefore aimed to study the association of DDIF decay times in two age groups: a younger group (4 subjects, 23y – 37y, mean age 27.3y) and an older group (5 subjects, 53 – 62y, mean age 56.3y). DDIF measurements were performed on the trabecular bone in the lumbar spine. An overview of the ages, gender, anatomic location and number of scans acquired is shown in Table 2.

DDIF sequence—For this pilot study, a single voxel MRS (SVS) DDIF pulse sequence was generously provided by Siemens Medical Systems (Erlangen, Germany) and installed on a Siemens Magnetom Avanto 1.5 T MRI scanner. To ensure that a true stimulated echo was acquired, the following measures were taken. A four step phase cycling scheme was implemented (Table 3) (13). In addition, crusher gradients were applied during the mixing time T_M to eliminate the formation of the first and second Hahn spin echoes. These crusher gradients do not affect the stimulated echo, because the spins that contribute to the stimulated echo are oriented along the longitudinal axis in the mixing period. Lastly, small spoiler gradients of 2 mT/m were applied for 5 msec in the encoding time periods, to dephase the FIDs signals elicited by the first and third RF pulses. The contribution of the imaging gradients of the DDIF sequence was calculated to be $T_s = 22$ sec (sequence gradients: 6 mT/m, 3 msec duration; spoiler gradients 2 mT/m, 5 msec duration), for water in bone marrow ($D = 0.5 \times 10^{-3}$ mm²/sec (33)). The SVS DDIF sequence was written to acquire all mixing times within one single acquisition.

MRI scanning—All subjects were scanned in supine position using the Siemens spine coil. A volume of interest was chosen in the L2 and/or L4/L5 vertebrae. As shown by Eq. 3, T_{DDIF} is influenced by the imaging gradients and T_1 . The contribution of the imaging gradients is constant for all DDIF acquisitions. The correlation between T_1 and age was investigated, to assess whether DDIF results require adjustment for changes in T_1 . Therefore, the scan protocol consisted of a SVS DDIF scan sequence as well as a SVS Inversion Recovery Spin Echo (IRSE) series for T_1 quantification.

SVS DDIF parameters: $T_{enc} = 10$ ms; $T_M = 20, 50, 100, 200, 400, 800$ ms; TR = 3000 ms; VOI = $20 \times 20 \times 20$ mm³; BW = 3000 Hz; number of samples = 256; 4-step phase cycling; number of averages (NSA) = 16 or 8; 4 dummy scans; Total scan time 5 minutes (NSA16) or 2 minutes 36 sec (NSA8). **SVS IRSE parameters:** TE = 30 ms; inversion time TI = 20, 200, 500, 700, 1000, 3000 ms; TR = 3000 ms; VOI = $20 \times 20 \times 20$ mm³; BW = 1000 Hz; number of samples = 512; number of averages = 8; total scan time 3 minutes 36 seconds.

Postprocessing of the DDIF and T_1 data—The water and fat peak areas of all DDIF and IRSE spectra were determined using a Lorentzian/Gaussian curve fitting tool (MATLAB peakfit.m (34)). For the DDIF scans, T_{DDIF} of the water and fat signals was found by a monoexponential fit to the normalized signal decay over T_M (29) using:

$$S = a_1 + a_2 e^{-\frac{t}{T_{DDIF}}} \quad [6]$$

The T_1 values for water and fat were calculated by fitting the area under the peaks in the IRSE spectra over the inversion time to the following signal model:

$$S = a_1 + a_2 \left| 1 + e^{-\frac{TR}{T_1}} - 2e^{-\frac{TI}{T_1}} \right| \quad [7]$$

To incorporate the influence of the bone marrow composition on the DDIF outcomes, the fat percentage of the bone marrow was determined for all subjects. The fat percentages were calculated from the DDIF spectrum with the shortest T_M (20 ms) by dividing the area of the fat peak by the sum of the areas of the water and fat peaks.

Results

Monte Carlo Simulations

The outcome of the simulations for the six bone models are shown in Figures 2-4. The magnetic field maps in ppm for the healthy (left column) and osteoporotic bone models (right column) are displayed in Figure 2. There is a clear distinction between the magnetic field distributions in the healthy versus the osteoporotic bone model. In the osteoporotic case, a more homogeneous field distribution can be appreciated within the pores. In addition, the increase of the marrow fat percentage from low to high (Fig. 2 top row to bottom row) results in an increase of magnetic field disturbances in the pore spaces. Close to the trabecular walls, the internal magnetic field values are around 0.2 – 0.3 ppm which agrees with results found by Sigmund *et al* (17).

These effects are also reflected in the magnetic field gradient distributions, shown in Figure 3. For all models, the maximum gradient strengths are found closest to the trabecular wall (layer 1) and are on the order of 0.2 – 0.3 ppm/voxel at a voxel size of $2 \times 2 \times 2 \mu\text{m}^3$. Moving away from the trabecular wall (from layer 1 towards layer 4), the gradient distributions shift toward lower gradient strengths, as exemplified by the distributions becoming more narrow. The changes in the solid bone structure are also reflected in the gradient distributions in the pore space: the osteoporotic model shows weaker field gradients in the pore space than the healthy bone model. Additionally, the marrow composition affects the gradient distributions: stronger magnetic field gradients are observed in the bone marrow models with higher fat percentage. This is expected given the larger susceptibility difference between solid bone and marrow in case of high marrow fat content.

The influence of trabecular bone structure and marrow composition changes on the gradient distribution is readily visible in the DDIF decay curves that are shown for all models in Figure 4a. The healthy bone and osteoporotic model results are shown by thick solid curves and thin dotted curves, respectively. The three marrow models are color coded: high fat percentage in red, medium fat percentage in yellow and low fat percentage in black. A trend with solid bone structure can be observed: the DDIF decay time increases when going from healthy to osteoporotic solid bone. In addition, the DDIF decay time decreases with increasing fat percentage in the bone marrow. The most striking result is the influence that marrow composition has on the DDIF outcome: the DDIF decay time of the healthy solid bone with the low fat percentage marrow shows high similarity to that of the osteoporotic solid bone with high fat percentage marrow. The T_{DDIF} values of all curves are plotted against fat percentage in Figure 4b for the healthy solid bone (green triangles) and osteoporotic bone (gray dots). Two separate trends can now be appreciated. First, T_{DDIF} decreases with increasing marrow fat, and second, the healthy solid bone and the osteoporotic solid bone are clearly distinct groups when sorted by the fat percentage of the bone marrow.

In vivo DDIF

T_1 results—Water and fat T_1 values are given in Table 4. No correlation was observed between age and T_1 values of water or fat, and no correlation was found between the T_1 values and the bone marrow fat percentage.

DDIF results—Typical *in vivo* SVS DDIF results are shown for subject #6 (age 54, L2 vertebra, fat percentage 21%) and subject #3 (age 25, L2 vertebra, fat percentage 33%) in Figure 5. On the left, the DDIF spectra for all T_M are shown. In these spectra, the water peak is downfield (on the left) and the fat peak upfield (on the right). The DDIF decay curves on the right show the integrals of the water peaks as a function of T_M (closed dots) and the monoexponential fits to these values (dotted line). For these two subjects, the T_{DDIF} are similar, the fat percentage of the bone marrow is not.

Next, the water DDIF decay time values were related to the fat percentage in the bone marrow, shown in Figure 6. All separate measurements are displayed (small markers), as well as the average values of T_{DDIF} and fat percentage per subject (large markers). A clear

relation between T_{DDIF} and fat percentage can be appreciated: DDIF decay times decrease with increasing fat percentage. Furthermore, a distinction between two age groups can be observed. The DDIF decay times of the younger group (green triangles) are lower than those of the older group (gray dots) for a given fat percentage. The trendlines in Figure 6 are based on all acquisitions per age group, and resulted in $R^2 = 0.75$ for the younger age group, and $R^2 = 0.65$ for the older age group.

The findings shown in Figure 6 are supported by the outcome of the Monte Carlo simulations, where a distinction between healthy and osteoporotic solid bone was observed when the influence of bone marrow composition was taken into account in the DDIF decay analysis.

Discussion and Conclusions

The work presented here advances DDIF MRI closer to clinical use as a tool to assess bone quality. The influence of the solid bone microstructure as well as bone marrow composition on the outcome of the DDIF technique was studied by Monte Carlo simulations and *in vivo* experiments in the lumbar spine in healthy volunteers.

Our results showed that DDIF MRI can differentiate healthy from osteoporotic solid bone structures. In addition, an important observation was made regarding bone marrow. Specifically, it was shown that the fat percentage of the bone marrow needs to be taken into account when analyzing DDIF data. By incorporating the marrow fat fraction into the analysis, the DDIF technique allowed for discrimination of healthy and osteoporotic bones in the Monte Carlo simulations and allowed for differentiation between a young and older age group in the *in vivo* experiments.

The *in vivo* study was designed as a preliminary investigation and included a small group of healthy subjects over a wide age range. No information on their medical history or living habits was obtained. Other factors that are known to influence bone quality and marrow composition (bone mineral density, smoking habits, hormone use, body composition, conditions such as obesity, metabolic diseases or eating disorders, physical activity, etc.) were not taken into account. In addition, there was no knowledge of bone marrow fat percentages prior to the imaging studies, making it difficult to stratify the results with respect to marrow composition with high statistical power. Within this heterogeneous group, a relation between age and T_{DDIF} was identified, taking into consideration the influence that marrow composition has on the DDIF technique. In our data, the distribution of T_{DDIF} values in the older age group was larger compared to the younger group. Accounting for health and lifestyle factors may identify with higher precision a relation between DDIF MRI, marrow composition and bone structure. A larger study relating DDIF MRI to detailed clinical information may provide additional insights, especially for the cases where intra-subject differences in DDIF decay times between the L2 and L4 vertebrae were observed.

A great advantage of the DDIF technique over direct spatial resolution of trabecular structure is that DDIF data do not need to be acquired at high spatial resolution. The current work has employed a spectroscopic version of DDIF in a volume of interest of $20 \times 20 \times 20$ mm³. There are multiple advantages to using a spectroscopic sequence. First, no fat

suppression is required. Since fat does not experience a DDIF effect, fat suppression would be required in an image based DDIF sequence to maximize the dynamic range of the DDIF signal variation (which occurs only in the water signal). Second, the results show that the fat percentage of the bone marrow plays an important role in the analysis of the DDIF outcome, and spectroscopy is the most accurate way to quantify fat content. Third, there is no need for high quality motion compensation and mechanical stabilization of the body region being scanned. Fourth, the DDIF acquisition time can be made quite short. In our study, the spectra acquired with 8 averages (2 minutes 36 sec) had sufficiently high SNR, suggesting a NSA reduction is possible. In addition, the total number of mixing times may be reduced to increase the speed of the sequence.

Since the DDIF sequence employs a quite long repetition time, it potentially allows for a multi-location SVS version of the sequence, where multiple vertebrae can be scanned simultaneously. Ultimately, a multi-location SVS DDIF sequence may provide a single measure per vertebrae, analogous to the DEXA technique, to diagnose osteoporosis and osteopenia.

In this work, the T_1 of water in the bone marrow was measured in all subjects to study the influence of the longitudinal relaxation on DDIF. It was observed that T_1 values are long compared to DDIF decay times and that no relation of T_1 over age or bone marrow fat percentage was found. This outcome suggests that in future applications of DDIF for bone quality measurements, T_1 measurements may be redundant.

Bone marrow is classified in two main types: red marrow which produces blood cells, and contains less fat, and yellow marrow containing mostly fat cells. The DDIF technique is based on the diffusion of water through the trabecular pore spaces and this may limit its applicability to anatomical regions where red marrow is present, such as the lumbar spine and femoral head.

For the purpose of the current work, studying the impact of changes in the solid bone and marrow composition on DDIF, we have chosen to generate all bone models by mathematical remodeling of a single native bone specimen to enable evaluation of such changes without the confounding influence of microstructural variations that would necessarily occur by obtaining separate specimens from healthy and osteoporotic individuals. With age, the overall trabecular bone volume fraction decreases (35). The exact microstructural changes of the trabecular bone are complex and differ between normal aging, postmenopausal osteoporosis and steroid induced osteoporosis (36). For the modeling of an osteoporotic solid bone mesh using the healthy bone specimen as a starting point, we chose the simplest bone loss method: uniform erosion. This method is not the best representation of the true biological progression of osteoporotic bone loss. Potential post-erosion occurrences of isolated islands of bone were not removed and anisotropic or strain-dependent effects were not incorporated. However it does mimic some of the basic features of osteoporosis such as trabecular thinning, loss of trabecular plates and an increase in bone surface to volume ratio, as shown in Table 1. Also, perforation occurs in our osteoporotic model. The concept of trabecular “plate” is only a crude approximation to the concave structures actually found in trabecular bone, and uniform thinning of a structural plate of uniform thickness will not lead

to its perforation. In contrast, uniform erosion of a native trabecular bone specimen will exhibit many of the known microstructural features of osteoporosis including thinning and perforation because native trabecular plates are actually concave.

The magnetic field distribution is calculated by convolution of the susceptibility distribution with the Green function, executed in the frequency domain. Discontinuities in the susceptibility distribution will therefore lead to high frequency fluctuations in the magnetic field distribution maps located at these abrupt susceptibility changes, which makes smoothing an essential part of the method. The μ CT data was acquired at 20 micron resolution and detailed structures at the boundary of the pore and solid bone at a sub 10 micron level are unknown to us. Smoothing the binary model reduces the high gradients which are not biological but rather are caused by the grid structure of the binary model due to limitations in spatial resolution.

In the Monte Carlo simulations, the magnetic susceptibility within the pores was modeled to be homogeneous. However, more complex distributions of fat and water within the pores can occur. There are multiple diseases which affect bone marrow compositions and fat spatial distributions in the pores. For instance, paratrabecular fat can be present, which constitutes of a layer of fat on the pore surfaces at the locations where the solid bone is lost (37), as is often seen in osteoporosis (37,38). In multiple myeloma and plasmacytoma, the opposite spatial arrangement may occur, where paratrabecular water is seen with islands of fat in the center of the pores (38). These heterogeneous spatial distributions of fat will have distinct influences on the internal field and will restrict the spaces in which water can diffuse (39). Since the DDIF technique is designed to probe this internal field by diffusion of water, it may therefore allow for discrimination of various bone marrow conditions which are characterized by specific spatial distributions of marrow fat as well as the bulk marrow composition.

Acknowledgments

The authors would like to thank Dr. Wolfgang Bogner for providing the SVS IRSE sequence, Dr. Ara Nazarian for the preparation of the trabecular bone samples and the μ CT measurements, and Dr. Dionyssios Mintzopoulos for his contributions to the DDIF pulse sequence development. Also, we want to thank Dr. Martin Torriani and Dr. Miriam Bredella for helpful discussions. Partial support was provided by Schlumberger-Doll Research, the Athinoula A. Martinos Center for Biomedical Imaging, and the Center for Functional Neuroimaging Technologies (funded by National Institutes of Health/National Institute of Biomedical Imaging and Bioengineering grant P41EB015896).

References

1. Parfitt AM, Mathews CH, Villanueva AR, Kleerekoper M, Frame B, Rao DS. Relationships between surface, volume, and thickness of iliac trabecular bone in aging and in osteoporosis. Implications for the microanatomic and cellular mechanisms of bone loss. *The Journal of clinical investigation*. 1983; 72(4):1396–1409. [PubMed: 6630513]
2. Genant HK, Cooper C, Poor G, Reid I, Ehrlich G, Kanis J, Nordin BE, Barrett-Connor E, Black D, Bonjour JP, Dawson-Hughes B, Delmas PD, Dequeker J, Ragi Eis S, Gennari C, Johnell O, Johnston CC Jr, Lau EM, Liberman UA, Lindsay R, Martin TJ, Masri B, Mautalen CA, Meunier PJ, Khaltayev N, et al. Interim report and recommendations of the World Health Organization Task-Force for Osteoporosis. *Osteoporos Int*. 1999; 10(4):259–264. [PubMed: 10692972]
3. Aaron JE, Johnson DR, Paxton S, Kanis JA. Secondary osteoporosis and the microanatomy of trabecular bone. *Clinical rheumatology*. 1989; 8(2):84–88. [PubMed: 2667873]

4. Bolotin HH. DXA in vivo BMD methodology: an erroneous and misleading research and clinical gauge of bone mineral status, bone fragility, and bone remodelling. *Bone*. 2007; 41(1):138–154. [PubMed: 17481978]
5. Bouxsein ML, Seeman E. Quantifying the material and structural determinants of bone strength. *Best practice & research*. 2009; 23(6):741–753. [PubMed: 19945686]
6. Inzerillo, AM.; Zaidi, M. *The Mount Sinai journal of medicine*. Vol. 69. New York: 2002. Osteoporosis: trends and intervention; p. 220-231.
7. Krug R, Carballido-Gamio J, Burghardt AJ, Kazakia G, Hyun BH, Jobke B, Banerjee S, Huber M, Link TM, Majumdar S. Assessment of trabecular bone structure comparing magnetic resonance imaging at 3 Tesla with high-resolution peripheral quantitative computed tomography ex vivo and in vivo. *Osteoporos Int*. 2008; 19(5):653–661. [PubMed: 17992467]
8. Wehrli FW. Structural and functional assessment of trabecular and cortical bone by micro magnetic resonance imaging. *J Magn Reson Imaging*. 2007; 25(2):390–409. [PubMed: 17260403]
9. Krug R, Stehling C, Kelley DA, Majumdar S, Link TM. Imaging of the musculoskeletal system in vivo using ultra-high field magnetic resonance at 7 T. *Investigative radiology*. 2009; 44(9):613–618. [PubMed: 19652609]
10. Wehrli FW, Hwang SN, Ma J, Song HK, Ford JC, Haddad JG. Cancellous bone volume and structure in the forearm: noninvasive assessment with MR microimaging and image processing. *Radiology*. 1998; 206(2):347–357. [PubMed: 9457185]
11. Newitt DC, Majumdar S, van Rietbergen B, von Ingersleben G, Harris ST, Genant HK, Chesnut C, Garnero P, MacDonald B. In vivo assessment of architecture and micro-finite element analysis derived indices of mechanical properties of trabecular bone in the radius. *Osteoporos Int*. 2002; 13(1):6–17. [PubMed: 11878456]
12. Wright AC, Lemdiasov R, Connick TJ, Bhagat YA, Magland JF, Song HK, Toddes SP, Ludwig R, Wehrli FW. Helmholtz-pair transmit coil with integrated receive array for high-resolution MRI of trabecular bone in the distal tibia at 7T. *J Magn Reson*. 2011; 210(1):113–122. [PubMed: 21402488]
13. Song YQ. Using Internal Magnetic Fields to Obtain Pore Size Distributions of Porous Media. *Concepts in Magnetic Resonance Part A*. 2003; 18A(2):97–110.
14. Song YQ, Ryu S, Sen PN. Determining multiple length scales in rocks. *Nature*. 2000; 406(6792): 178–181. [PubMed: 10910355]
15. Hurlimann MD. Effective Gradients in Porous Media Due to Susceptibility Differences. *J Magn Reson*. 1998; 131(2):232–240. [PubMed: 9571098]
16. Song YQ. Pore sizes and pore connectivity in rocks using the effect of internal field. *Magnetic resonance imaging*. 2001; 19(3-4):417–421. [PubMed: 11445322]
17. Sigmund EE, Cho H, Song YQ. High-resolution MRI of internal field diffusion-weighting in trabecular bone. *NMR in biomedicine*. 2009; 22(4):436–448. [PubMed: 19023866]
18. Sigmund EE, Cho H, Chen P, Byrnes S, Song YQ, Guo XE, Brown TR. Diffusion-based MR methods for bone structure and evolution. *Magn Reson Med*. 2008; 59(1):28–39. [PubMed: 18098292]
19. Vande Berg BC, Lecouvet FE, Moysan P, Maldague B, Jamart J, Malghem J. MR assessment of red marrow distribution and composition in the proximal femur: correlation with clinical and laboratory parameters. *Skeletal radiology*. 1997; 26(10):589–596. [PubMed: 9361354]
20. Cristy M. Active bone marrow distribution as a function of age in humans. *Physics in medicine and biology*. 1981; 26(3):389–400. [PubMed: 7243876]
21. Ishijima H, Ishizaka H, Horikoshi H, Sakurai M. Water fraction of lumbar vertebral bone marrow estimated from chemical shift misregistration on MR imaging: normal variations with age and sex. *Ajr*. 1996; 167(2):355–358. [PubMed: 8686603]
22. Justesen J, Stenderup K, Ebbesen EN, Mosekilde L, Steiniche T, Kassem M. Adipocyte tissue volume in bone marrow is increased with aging and in patients with osteoporosis. *Biogerontology*. 2001; 2(3):165–171. [PubMed: 11708718]
23. Shen W, Chen J, Gantz M, Punyanitya M, Heymsfield SB, Gallagher D, Albu J, Engelson E, Kotler D, Pi-Sunyer X, Shapses S. Ethnic and sex differences in bone marrow adipose tissue and bone mineral density relationship. *Osteoporos Int*. 23(9):2293–2301. [PubMed: 22173789]

24. Bredella MA, Fazeli PK, Miller KK, Misra M, Torriani M, Thomas BJ, Ghomi RH, Rosen CJ, Klibanski A. Increased bone marrow fat in anorexia nervosa. *The Journal of clinical endocrinology and metabolism*. 2009; 94(6):2129–2136. [PubMed: 19318450]
25. Schellinger D, Lin CS, Fertikh D, Lee JS, Lauerman WC, Henderson F, Davis B. Normal lumbar vertebrae: anatomic, age, and sex variance in subjects at proton MR spectroscopy--initial experience. *Radiology*. 2000; 215(3):910–916. [PubMed: 10831721]
26. Yeung DK, Griffith JF, Antonio GE, Lee FK, Woo J, Leung PC. Osteoporosis is associated with increased marrow fat content and decreased marrow fat unsaturation: a proton MR spectroscopy study. *J Magn Reson Imaging*. 2005; 22(2):279–285. [PubMed: 16028245]
27. Hopkins JA, Wehrli FW. Magnetic susceptibility measurement of insoluble solids by NMR: magnetic susceptibility of bone. *Magn Reson Med*. 1997; 37(4):494–500. [PubMed: 9094070]
28. Schenck JF. The role of magnetic susceptibility in magnetic resonance imaging: MRI magnetic compatibility of the first and second kinds. *Medical physics*. 1996; 23(6):815–850. [PubMed: 8798169]
29. Mintzopoulos D, Ackerman JL, Song YQ. MRI of trabecular bone using a decay due to diffusion in the internal field contrast imaging sequence. *J Magn Reson Imaging*. 2011; 34(2):361–371. [PubMed: 21780229]
30. Hahn EL. Spin Echoes. *Physical Review*. 1950; 80(4):580–594.
31. Sprinkhuizen SM, Konings MK, van der Bom MJ, Viergever MA, Bakker CJ, Bartels LW. Temperature-induced tissue susceptibility changes lead to significant temperature errors in PRFS-based MR thermometry during thermal interventions. *Magn Reson Med*. 64(5):1360–1372. [PubMed: 20648685]
32. Carr HY, Purcell EM. Effects of Diffusion on Free Precession in Nuclear Magnetic Resonance Experiments. *Physical Review*. 1954; 94(3)
33. Yeung DK, Wong SY, Griffith JF, Lau EM. Bone marrow diffusion in osteoporosis: evaluation with quantitative MR diffusion imaging. *J Magn Reson Imaging*. 2004; 19(2):222–228. [PubMed: 14745757]
34. O'Haver, T. [Accessed July 2013] Interactive Peak Fitter. Published May 2008 <http://terpconnectumdedu/~toh/spectrum/InteractivePeakFitter.htm>
35. Mosekilde L. Sex differences in age-related loss of vertebral trabecular bone mass and structure--biomechanical consequences. *Bone*. 1989; 10(6):425–432. [PubMed: 2624823]
36. Dalle Carbonare L, Arlot ME, Chavassieux PM, Roux JP, Portero NR, Meunier PJ. Comparison of trabecular bone microarchitecture and remodeling in glucocorticoid-induced and postmenopausal osteoporosis. *J Bone Miner Res*. 2001; 16(1):97–103. [PubMed: 11149495]
37. Allen JE, Henshaw DL, Keitch PA, Fewes AP, Eatough JP. Fat cells in red bone marrow of human rib: their size and spatial distribution with respect to the radon-derived dose to the haemopoietic tissue. *International journal of radiation biology*. 1995; 68(6):669–678. [PubMed: 8551110]
38. Burkhardt R, Kettner G, Bohm W, Schmidmeier M, Schlag R, Frisch B, Mallmann B, Eisenmenger W, Gilg T. Changes in trabecular bone, hematopoiesis and bone marrow vessels in aplastic anemia, primary osteoporosis, and old age: a comparative histomorphometric study. *Bone*. 1987; 8(3):157–164. [PubMed: 3606907]
39. Capuani S. Water diffusion in cancellous bone. *Microporous and Mesoporous Materials*. 2013; 178:34–38.

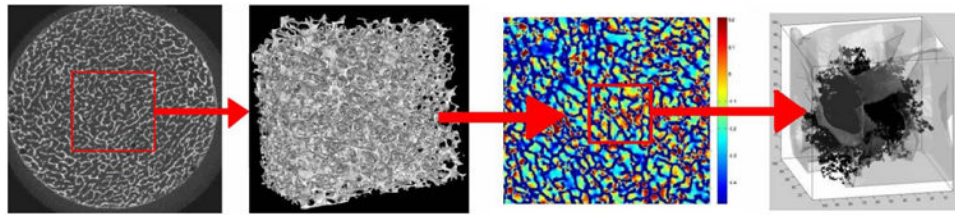


Figure 1. Monte Carlo model preparation steps for the trabecular bone μ CT data. From left to right: transverse μ CT slice; rendered volume of 10.24 mm^3 taken from the center of binarized μ CT data, within which the magnetic field distribution was calculated; example slice of the magnetic field map; example of 100 random walks (black lines) within the trabecular bone volume. [Color figure can be viewed in the online issue, which is available at wileyonlinelibrary.com.]

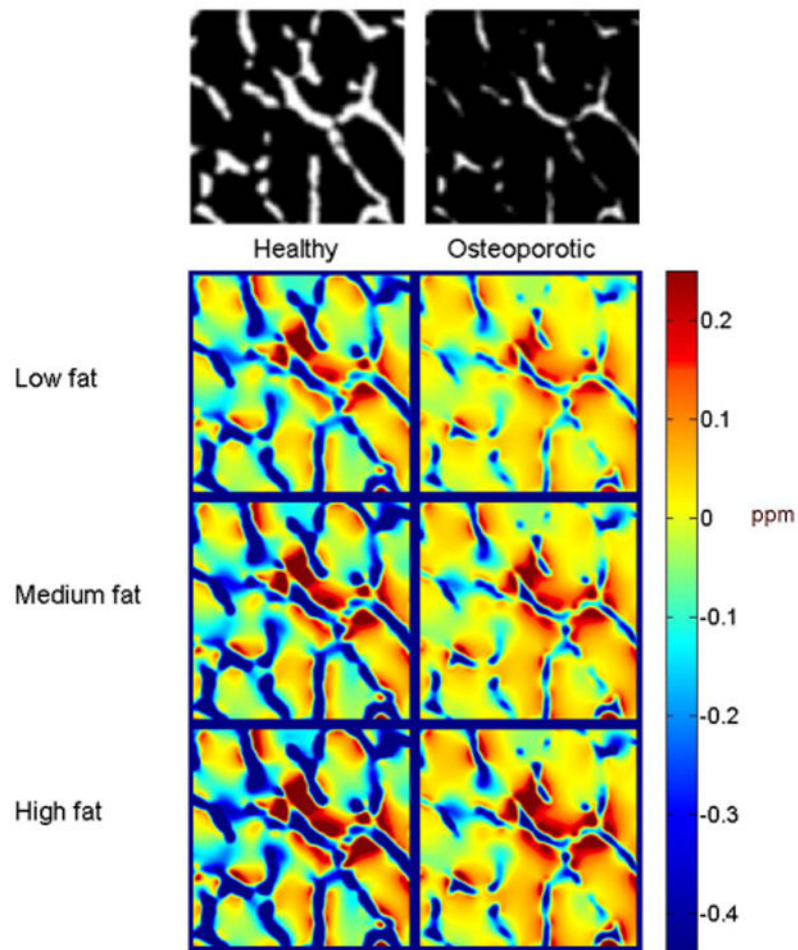


Figure 2. Magnetic field maps (ppm) in the six trabecular bone models. The healthy (left) and osteoporotic (right) solid bone models are shown the top row. Magnetic field changes increase with increasing bone marrow fat percentage (top to bottom).

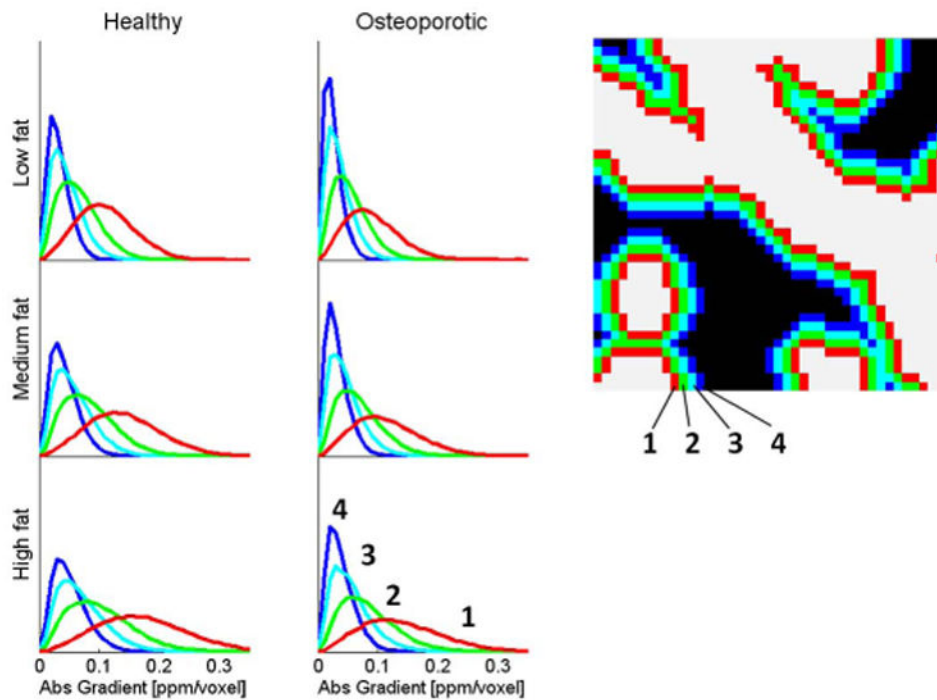


Figure 3.

Magnetic field gradient histograms in the six trabecular bone models of four layers in the pore space. Regions were defined by a single-voxel width layer in the pore space, starting at the trabecular wall (layer 1) and moving inwards into the pore space (layer 2-4). A zoomed in region of the bone model and the 4 color coded layers is shown top right. [Color figure can be viewed in the online issue, which is available at wileyonlinelibrary.com.]

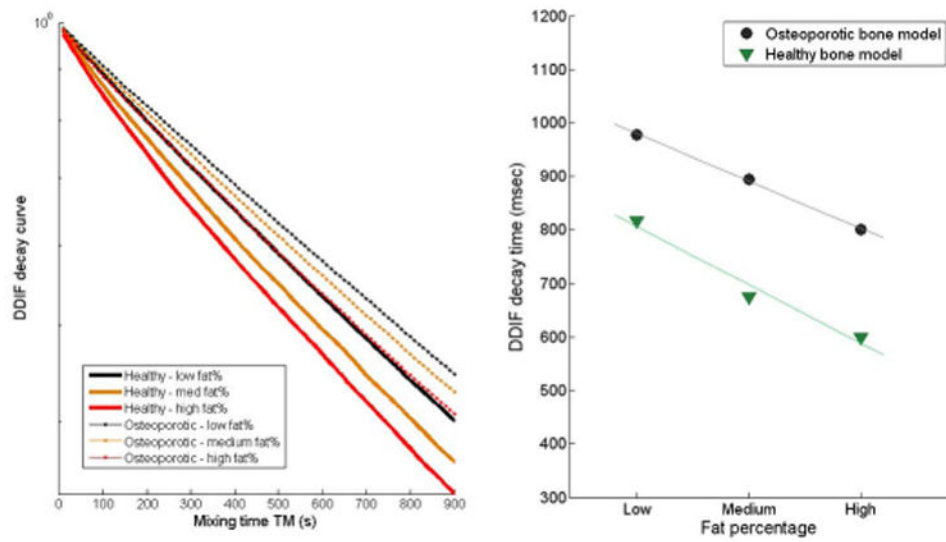


Figure 4. Outcome of the Monte Carlo simulations. DDIF decay curves for all six trabecular bone models (left) and DDIF decay time values versus bone marrow fat percentage for the healthy trabecular bone models (green triangles) and osteoporotic models (gray dots). [Color figure can be viewed in the online issue, which is available at wileyonlinelibrary.com.]

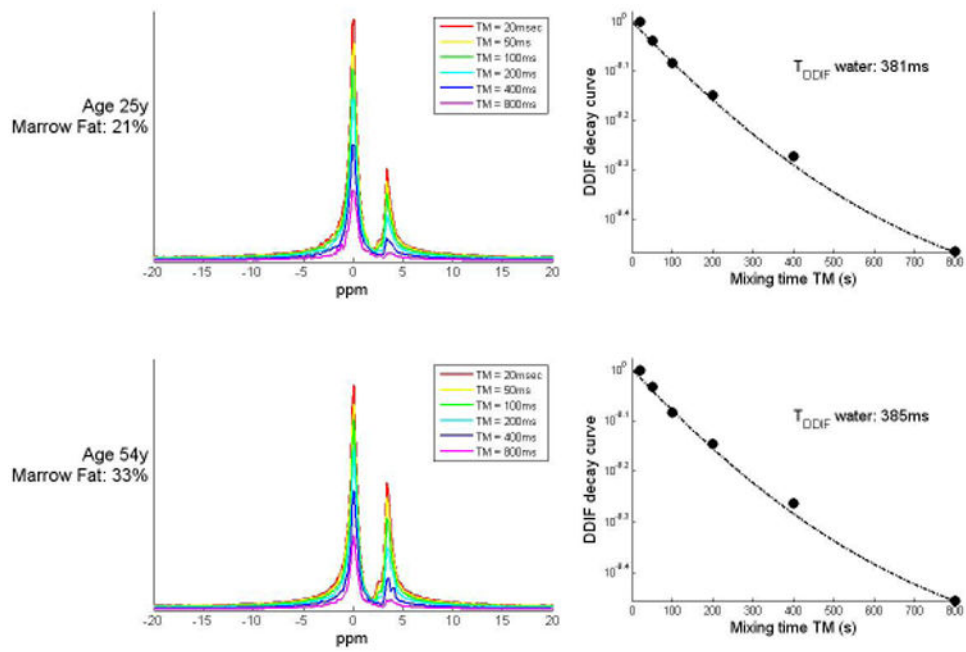


Figure 5.

In vivo DDIF results. The DDIF spectra (left) for all 6 mixing times and DDIF decay values over mixing time and the monoexponential fit (right) are shown for a young subject with marrow fat of 21% (top row) and older subject with marrow fat of 33% (bottom row). [Color figure can be viewed in the online issue, which is available at wileyonlinelibrary.com.]

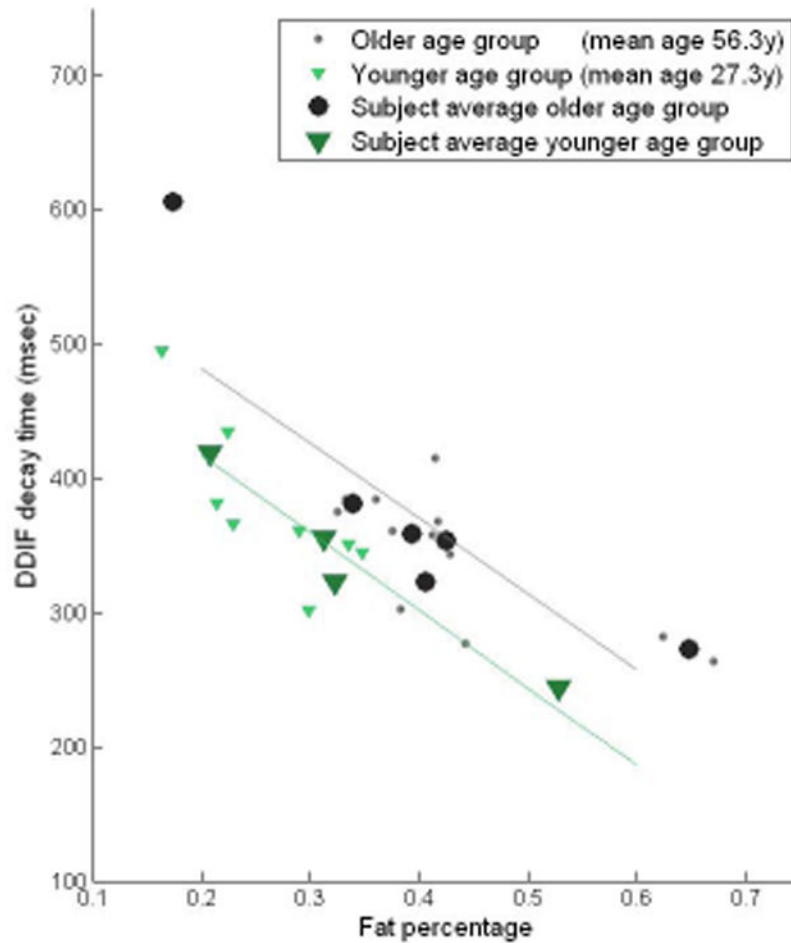


Figure 6.

T_{DDIF} versus bone marrow fat percentage for subjects in the younger age group (green triangles) and older age group (gray dots). A clear correlation of T_{DDIF} with fat percentage can be appreciated, as well as a difference in T_{DDIF} values between the two age groups for a given bone marrow fat percentage. Trendlines were based on all data points per age group: younger age group $R^2 = 0.75$, older age group $R^2 = 0.65$. [Color figure can be viewed in the online issue, which is available at wileyonlinelibrary.com.]

Table 1

Microstructural properties of the healthy and osteoporotic bone model.

Model (BV/TV %)	BS/BV	Tb.Th (mm)	Tb.N (1/mm)	Tb.Sp (mm)
<i>Healthy bone model (19%)</i>	x	0.058	3.31	0.24
	y	0.053	3.63	0.22
	z	0.078	2.45	0.33
	Average	0.061	3.13	0.26
<i>Osteoporotic bone model (7%)</i>	x	0.035	1.99	0.47
	y	0.031	2.26	0.41
	z	0.049	1.41	0.66
	Average	0.037	1.88	0.49

BV = Material volume; TV = Total volume; BV/TV = Material volume fraction; BS = Bone surface; BS/BV = Bone surface to bone volume ratio; Tb.Th = Trabecular plate thickness; Tb.N = Trabecular plate number; Tb.Sp = Trabecular plate separation.

Table 2

Overview of the age, gender and scanned location of the subjects.

Subject #	Age	Gender	Location (# scans per location)
1	23	F	L2 (1)
2	24	M	L2 (1), L4 (1)
3	25	F	L2 (2), L4 (2)
4	37	F	L2 (1), L4 (1)
5	53	F	L2 (1), L4 (1)
6	54	F	L2 (2), L4 (1)
7	56	F	L2 (2), L4 (1)
8	56	F	L2 (1), L5 (1)
9	57	F	L2 (1), L4 (1)
10	62	F	L2 (1)

Table 3

Phase cycling scheme for the DDIF sequence.

	RF1	RF2	RF3	ADC
1	90	0	0	0
2	270	0	0	180
3	90	180	0	180
4	270	180	0	0

Table 4

T_1 values for water and fat in bone marrow in the lumbar spine of healthy volunteers at 1.5 T. In case T_1 was measured in both L2 and L4/L5, the average T_1 value is given.

Subject #	Age	T_1 water (ms)	T_1 fat (ms)
1	23	1370	287.0
2	24	1232	283.6
3	25	1253	279.9
4	37	1230	282.3
5	53	1235	284.4
6	54	1325	272.9
7	56	1282	278.6
8	56	1310	286.8
9	57	1224	285.5
10	62	1165	274.5
Average		1263 ± 60	281.6 ± 5.0